ARTICLE TYPE

Journal of Materials Chemistry A Accepted Manuscript

Earth-abundant and Nano-micro composite catalysts of Fe₃O₄@Reduced Graphene Oxide for Green and Economical Mesoscopic Photovoltaics with High Efficiencies up to 9%

Huawei Zhou[a], Jie Yin[b*], Xianxi Zhang[a], Zhaojin Yang[b], Dongjie Li[b], Junhu Wang[c], Xin Liu[c], Changzi Jin[c], Tingli Ma[d]

The ideal liquid-solid heterogeneous electrocatalysis should have not only high catalytic activity but also free electron transport. However, preparing a single catalyst that simultaneously possesses both advantages has proven to be challenging. Herein, we prepared nano-micro composite catalysts (NMCC) composed of highly dispersed Fe₃O₄ nanoparticles fixed on reduced graphene oxide (RGO) sheets (namely, Fe₃O₄@RGO-NMCC) as counter electrode (CE) in dye-sensitized solar cells (DSCs). Compared with Fe₃O₄ or RGO CE, Fe₃O₄@RGO-NMCC CE exhibited improved activity and reversibility for the catalytic reduction of triiodide ions (I_3^-) into iodide ions (I^-). Notably, DSCs using rigid and flexible Fe₃O₄@RGO-NMCC CEs achieved high PCEs up to 9% and 8% on fluorine-doped tin oxide (FTO)/glass substrates and flexible polymer substrates, respectively. These values are, to our knowledge, one of the highest reported efficiencies for DSCs based on a flexible Pt-free CE. We ascribed the superior catalytic performance of Fe₃O₄@RGO-NMCC to faster electron hopping between Fe^{2+} and Fe^{3+} and free electron transport by broad RGO sheets. Finally, Fe₃O₄@RGO-NMCC exhibited good stability in practical application of DSCs because Fe₃O₄ nanoparticles were chemically bonded to the surface of RGO. Our work here will be great interest for fundamental research and practical applications of Fe₃O₄ in lithium battery, spliting-water and magnetic fields.

Introduction

As third-generation photovoltaic devices, dye-sensitized solar cells (DSCs)[1] based on environment-friendly (i.e., green) raw materials completely free of Cd or Pb, have been regarded as very promising solar cells owing to their simple synthesis procedures, high theoretical power conversion efficiency (PCE), and low cost. With continuous efforts from researchers worldwide, the PCEs of DSCs have been improved by 13%[2] using Pt as the counter electrode (CE).

As key components, CEs of DSCs are used to collect electrons from the external circuit, and more importantly, catalyze the reduction of redox mediators in electrolyte. Pt is the most widely used CE material in DSCs. However, using Pt involves a number of challenges. First, the scarcity and high cost of Pt cannot meet the needs of mass industrial production. Secondly, Pt can be corroded by I^-/I_3^- electrolytes, leading to poor stability of the photovoltaic device.[3,4] Therefore, developing a high-performance, low-cost, corrosion-resistant, non-precious metal catalyst is necessary. In recent years, numerous researchers have developed alternative CE materials, such as inorganic materials,[5,6] carbon materials,[7-10] and conductive polymer materials[11,12].

Of the transition metal oxides studied, iron oxides showed remarkable abundance and notable catalytic activity, with PCEs of 6.89% for Fe₂O₃ nanoparticles[13] and 7.65% for Fe₃O₄ hierarchical structures[14]. However, grain boundaries in nanoparticle and hierarchical structures are massive and remarkably hinder electron transport.[15,16] Recently, our group further synthesized a composite catalyst of rosin carbon/Fe₃O₄ to enhance the performance of the corresponding DSCs[17]. However, the Fe₃O₄ nanoparticle on rosin carbon substantially aggregates together, resulting in loss of the active sites.

Herein, we prepared nano-micro composite catalysts (NMCC) composed of highly dispersed Fe₃O₄ nanoparticles fixed on reduced graphene oxide (RGO) sheets (namely, Fe₃O₄-NMCC) as CE in DSCs. Compared with pure Fe₃O₄ and RGO CE, Fe₃O₄@RGO-NMCC CE exhibited improved activity and reversibility for the catalytic reduction of triiodide (I_3^-) into iodide (I^-). Notably, DSCs using rigid and flexible Fe₃O₄@RGO-NMCC CEs achieved high PCEs up to 9% and 8% on fluorine-doped tin oxide (FTO)/glass substrates and flexible polymer substrates, respectively. These values are, to our knowledge, the highest reported efficiencies for DSCs based on a flexible Pt-free CE. We ascribed the superior catalytic performance of Fe₃O₄@RGO-NMCC to faster electron hopping between Fe^{2+} and Fe^{3+} and free electron transport by broad RGO sheets. Finally, Fe₃O₄@RGO-NMCC exhibited good stability in practical
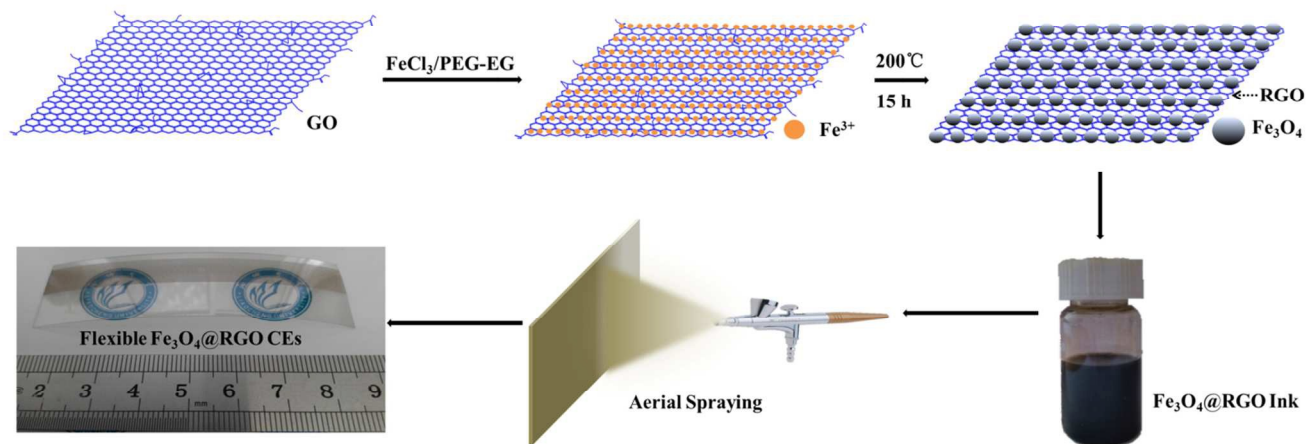
Scheme 1. Schematic diagrams to illustrate simple methods for preparing Fe_3O_4@RGO (reduced graphene oxide) nano-micro composite catalysts by one-pot solvothermal approach and fabrication of flexible Fe_3O_4@RGO counter electrodes by aerial spraying.

5

application of DSCs because Fe_3O_4 nanoparticles were chemically bonded to the surface of RGO.

Experimental Section

Preparation of Fe_3O_4: Typically, 10ml 0.5 molL^{-1} FeCl$_3$ in
10 ethylene glycol (EG) solution, 10 ml 0.1 gmL^{-1} polyethylene glycol (PEG) in EG solution and 10 ml 1.5 molL^{-1} NaOH in EG solution were mixed. The mixture was stirred for 4 h at room temperature and then transferred into a teflon-lined autoclave. After being heated at 200 °C for 15 h, the mixture was cooled to
15 room temperature naturally.

Preparation of RGO:

Graphene oxide (GO) was prepared using a modified Hummers method. Typically, flake graphite (1 g), sodium nitrate (1 g), and potassium permanganate (3.0 g) were mixed in 98% sulfuric acid
20 (48 mL) by vigorous agitation in a roundbottom flask at 0 ° C for 24 h. Then, the mixture was heated and kept at 35 ° C for 30 mins. After that, 250 ml distilled water was slowly added into the suspension and stirred for 20 min. Then, 2.5 mL hydrogen peroxide (30%) was added into the mixture. The as-prepared
25 suspension was washed thoroughly with deionized water and centrifuged with 3000 rpm. After that, the supernatant was then centrifuged with 8000 rpm until its pH was ≈ 7. The obtained precipitates were redispersed in deionized water to obtain a 1.7 wt% GO dispersion. 27 g 1.7 wt% GO dispersion were dispersed
30 in 100 ml EG solution. The mixture was stirred for 4 h at room temperature and then transferred into a teflon-lined autoclave. After being heated at 200 °C for 15 h, the mixture was cooled to room temperature naturally.

Preparation of Fe_3O_4@RGO-NMCC: Typically, 10ml 0.5
35 molL^{-1} FeCl$_3$ in EG solution, 10 ml 0.1 gmL^{-1} PEG in EG solution and 10 ml 1.5 molL^{-1} NaOH in EG solution were mixed with 2.7g 1.7 wt% GO aqueous solution dispersed in 10 ml EG solution. The mixture was stirred for 4 h at room temperature and then transferred into a teflon-lined autoclave. After being heated
40 at 200 °C for 15 h, the mixture was cooled to room temperature

naturally.

Photoanode preparation and cell fabrication: A layer of 20 nm-sized TiO$_2$ (P25, Degussa, Germany) layer (12 μm) was loaded on FTO glass by printing technique method and used in
45 this study[10]. The obtained film was sintered at 500 °C. After cooling to 90 °C, the TiO$_2$ films were immersed in a solution of N719 dye (5 x 10^{-4} M) in acetonitrile/tert-butyl alcohol (1:1 volume ration) for 20 h. For the TiO$_2$ photoanode film treated by TiCl$_4$, the films were immersed in 40 mM TiCl$_4$ solution at 70°C
50 for 30 mins and then sintered at 500 °C for 30 mins. The triiodide/iodide electrolyte for cell testing is composed of LiI (0.03 M), 1-butyl-3-methylimidazolium iodide (0.6 M), I$_2$ (0.03 M), 4-tert-butyl pyridine (0.5 M), guanidinium thiocyanate in acetonitrile (0.1 M). DSCs were assembled by a TiO$_2$ photoanode
55 with corresponding counter electrode sandwiching redox couple in the electrolyte. The symmetrical cells with effective area (0.64 cm^2) were carried out in the Tefal-polarization test and the EIS experiments.

Characterization: To analyze the composition of as-synthesized
60 samples, we obtained X-ray diffraction (XRD) patterns using PANalytical X´Pert diffractometer (Cu Kα radiation at λ = 1.54 Å) sampling at 8°/ min, 40 kV and 100 mA. The as-prepared micro or nanostructures were characterized and analyzed by scanning electron microscopy (SEM, Nova Nano SEM 450), transmission
65 electron microscopy (TEM, FEI Tecnai G2 F30) with an accelerating voltage (300 Kv). The Mössbauer spectrum of the as-prepared materials were recorded using a Topologic 500A spectrometer and a proportional counter at room temperature. ^{57}Co(Rh) moving in a constant acceleration mode was used as
70 radioactive source. The films thicknesses were measured using film-thickness measuring device (KLA-Tencor D-100). The photocurrent–voltage performance of DSCs with 0.16 cm^2 photoanode film were measured without metal mask by a Keithley digital source meter (Keithley 2400, USA) and equipped
75 with a solar simulator (IV5, PV Measurements, Inc., USA). IPCE of DSCs were measured by the quantum efficiency/spectral response(SR)/incident photon to current conversion efficiency (IPCE) measurement system (QEX10, PV Measurements, Inc.,

USA). EIS experiments were measured in the dummy cells in the dark using a computer-controlled potentiostat (Zennium Zahner, Germany). Cyclic voltammetry (CV) was measured in a three-electrode system. The triiodide/iodide electrolyte for CV testing is composed of LiI (2 mM), LiClO$_4$ (20 mM) and I$_2$ (0.2 mM).

Results and Discussions

In our experiments, Fe$_3$O$_4$@RGO-NMCC was prepared using a simple one-pot solvothermal approach as shown in Scheme 1. Details of the preparation can be seen in the experimental section. SEM images in Figure S1 and S2 illustrated the agglomerated structure of pure Fe$_3$O$_4$ particles and two-dimensional structure of RGO. TEM image in Figure 1a further showed the agglomeration of pure Fe$_3$O$_4$ particles resulting in the ununiform size of the particles or caking within the range of 50 nm to 330 nm (Figure 1b). The agglomerated structure embedded catalytic active sites. In addition, the massive grain boundaries in pure Fe$_3$O$_4$ inhibited electron transport.[15,16] These two factors decreased catalytic activity of pure Fe$_3$O$_4$ particles. The transmission electron microscopy (TEM) image of Fe$_3$O$_4$@RGO-NMCC (Figure 1c) showed that Fe$_3$O$_4$ nanoparticles were highly dispersed and firmly fixed on the surface of RGO, thus preventing agglomeration. The sizes of Fe$_3$O$_4$ nanoparticles on RGO were well within the range of 10 nm to 30 nm, with an average particle size of 19 nm (Figure 1d). X-ray diffraction patterns of these samples (Figure 1e) showed that Fe$_3$O$_4$@RGO-NMCC displays a crystalline structure similar to that of pure Fe$_3$O$_4$, which could be indexed to the standard Fe$_3$O$_4$
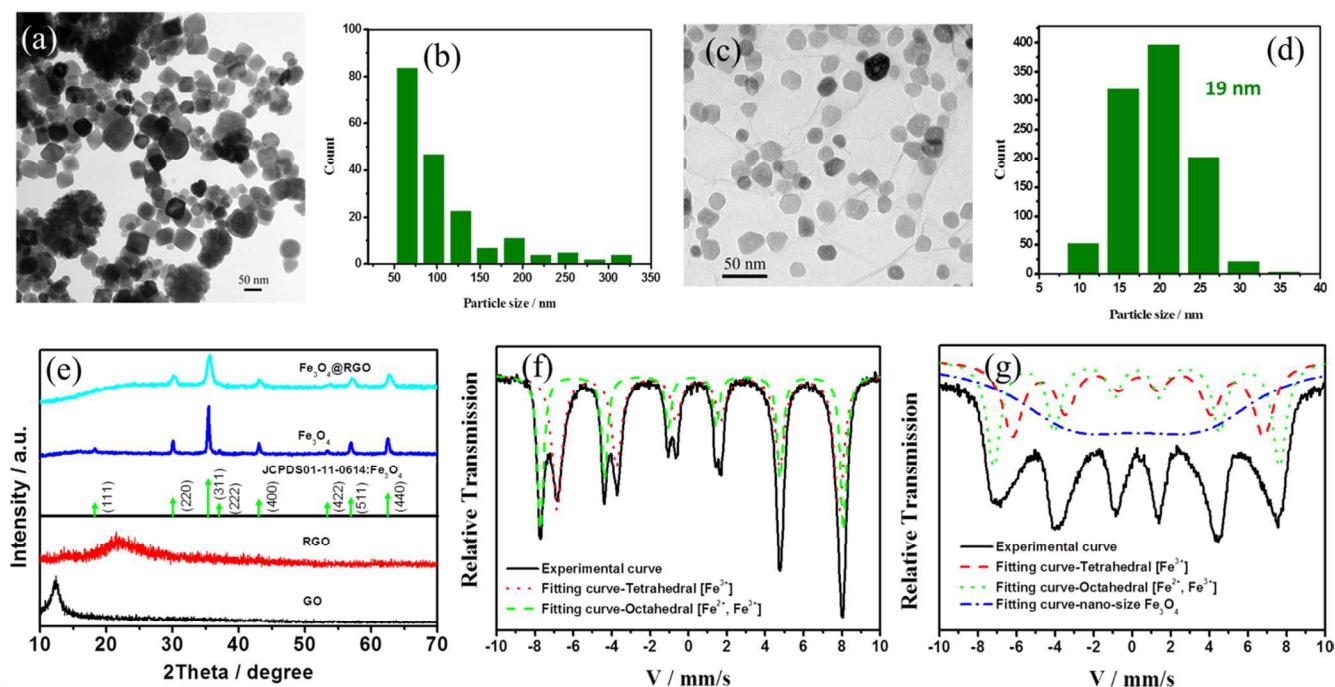
Figure 1. (a) TEM images of the as-prepared pure Fe$_3$O$_4$ agglomerated nanoparticles; (b) size distribution of pure Fe$_3$O$_4$ agglomerated nanoparticles. (c) TEM images of Fe$_3$O$_4$@RGO nano-micro composite catalysts; (d) size distribution of highly dispersed Fe$_3$O$_4$ nanoparticles in Fe$_3$O$_4$@RGO nano-micro composite catalysts; (e) XRD patterns of as-prepared GO, RGO, Fe$_3$O$_4$, Fe$_3$O$_4$@RGO powder; (f) the Mössbauer spectrum of as-prepared pure Fe$_3$O$_4$ agglomerated nanoparticles; (g) the Mössbauer spectrum of as-prepared Fe$_3$O$_4$@RGO nano-micro composite catalysts

nanocrystal with a cubic structure (JCPDS01-11-0614). The diffraction peaks of 30.1°, 35.4°, 37.1°, 43.1° 54.3°, 57.0°, and 62.5° were attributed to the planes of (220), (311), (222), (400), (422), (511), and (440) of Fe$_3$O$_4$, respectively. In addition, the peak width of Fe$_3$O$_4$@RGO-NMCC was larger compared with that of pure Fe$_3$O$_4$, indicating the decrease in size of Fe$_3$O$_4$ on RGO. This finding was consistent with the SEM result. Mössbauer spectroscopy was performed to examine the super-fine structure in pure Fe$_3$O$_4$ and Fe$_3$O$_4$@RGO. The energy resolution of the Mössbauer spectrum was very high and was used to study the ultrafine interaction between the atomic nucleus and the surrounding environment. The Mössbauer spectrum of pure Fe$_3$O$_4$ could be fitted into two fitting curves, which were associated with the tetrahedral [Fe^{3+}] ions and the octahedral [Fe^{2+}, Fe^{3+}] in inverse spinel structure[18]. In contrast to pure Fe$_3$O$_4$, the Mössbauer spectrum of Fe$_3$O$_4$@RGO-NMCC was fitted to three fitting curves. Among the three fitting curves, two fitting curves corresponded to the tetrahedral [Fe^{3+}] ions and the octahedral [Fe^{2+}, Fe^{3+}] in pure Fe$_3$O$_4$. The relatively wide curve fitting was due to the reduced nano-size effect of Fe$_3$O$_4$ in Fe$_3$O$_4$@RGO-NMCC, which resulted in higher surface energy, enhanced quantum effect, faster electronic hopping between [Fe^{2+}] and [Fe^{3+}], and stronger relaxation effect (as in dangling bonds). Compared to the large size of pure Fe$_3$O$_4$, The higher surface energy of the reduced nano-size effect of Fe$_3$O$_4$ in Fe$_3$O$_4$@RGO-NMCC originated from more unsaturated bonds of surface atomic, which are active site to absorb and catalysis "I$_3^-$" to "I$^-$". Enhanced quantum effect was attributed to the increased atom

density of the surface Fe^{2+} and Fe^{3+}, which promoted electronic transport (hopping) in electro-catalysis reaction "$I_3^- + 2e^- \leftrightarrow 3I^-$". Thus, these structural effects enhanced the catalytic activity of Fe_3O_4@RGO-NMCC.

5   The thickness of counter electrode influences the catalytic activity. Different thicknesses of CEs were prepared by spraying different volume of Fe_3O_4@RGO-NMCC dispersion onto FTO glass substrate. Figure S3 showed the current density (J)–voltage (V) characteristics of DSCs based on different thickness of 10 Fe_3O_4@RGO-NMCC CEs. The detailed photovoltaic parameters were shown in Table S1. The photovoltaic devices with approximately 16 μm thickness of Fe_3O_4@RGO-NMCC CEs have the best performance. As reference, the same thicknesses of Fe_3O_4 and RGO were then fabricated into CEs by spraying onto 15 FTO glass substrate. First, the photovoltaic performance was obtained by characterizing DSCs based on these three CEs under AM1.5, 100 mW cm^{-2} simulated illumination. For each CE, we fabricated four DSC devices and obtained the mean photovoltaic

performance. The detailed photovoltaic parameters are 20 summarized in Table 1. Figure 2a shows the best photocurrent density with respect to voltage (J–V curve) for the DSCs in each group. The DSCs based on Fe_3O_4@RGO-NMCC CEs presented a PCE of 6.76%, the highest among the three CEs. Compared with DSCs based on Fe_3O_4@RGO-NMCC CEs, open-circuit voltage 25 (V_{oc}) and short-circuit current density (J_{sc}) slightly decreased for DSCs based on Fe_3O_4 and RGO CEs. Thus, the main factor leading to low PCEs (from 6.76% to 1.92% and 3.71%) were derived from the deterioration of the fill factors of DSCs based on Fe_3O_4 and RGO CEs (from 0.62 to 0.39 and 0.22). Among the 30 factors determining photovoltaic parameters of the DSCs, large internal resistance and low catalytic activity caused a decrease in fill factor and PCE. A large interparticle boundary in Fe_3O_4 adversely affected the electron transfer, further increasing the internal resistance of devices, and the less active sites in the RGO 35 should be the reason of the low fill factor of the photovoltaic
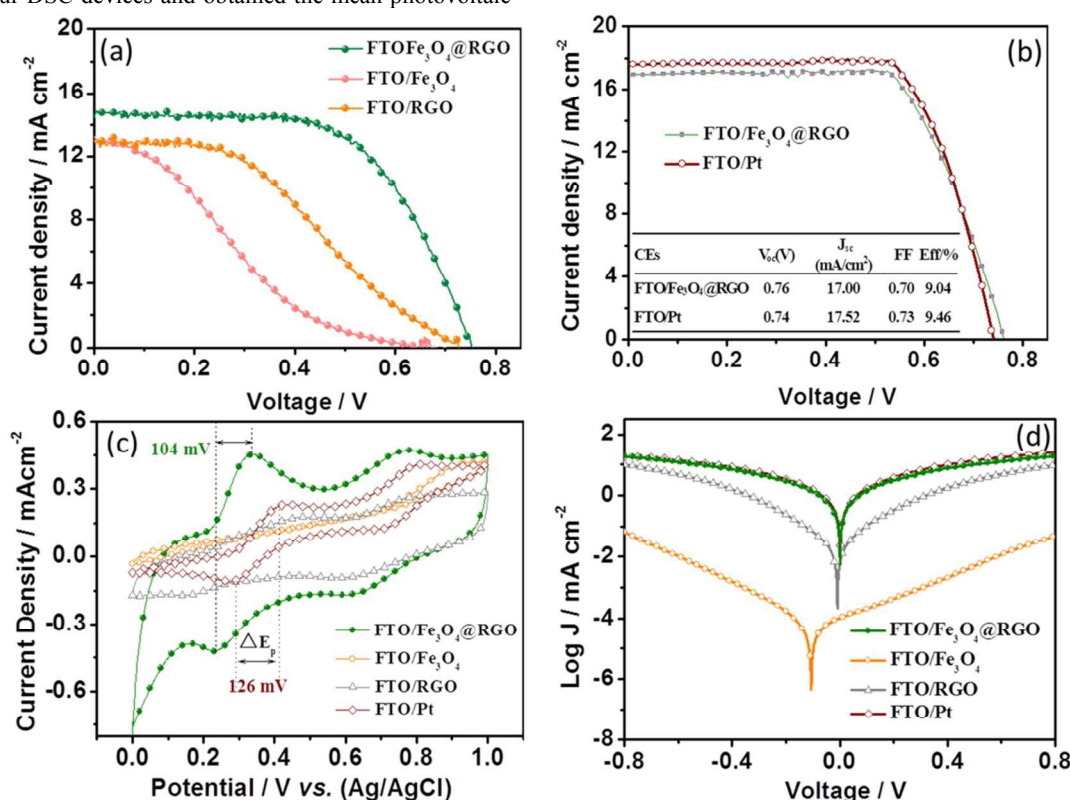
Figure 2. Photovoltaic and electrochemical properties characterization of CEs fabricated on FTO substrate: (a) *J-V* curves of DSCs based on these three CEs under AM1.5, 100 mW cm^{-2} simulated illumination. (b) *J-V* curves of DSCs optimized by TiCl$_4$ treatment. (c) Tafel polarization curves of the I_3^-/I^- symmetrical cells fabricated with two identical CEs (CE/electrolyte/CE); (d) CV curves of various CEs in 40 liquid electrolyte (I_3^-/I^-) system of DSCs.

Table 1. Photovoltaic parameters of the DSCs without TiCl$_4$ treatment for each group (four DSC devices)

CE	V_{oc}(V)	J_{sc}(mA/cm^2)	FF	PCE/%
Fe_3O_4/RGO	0.76 ±0.01	14.4 ±0.1	0.62±0.01	6.76±0.05
Fe_3O_4	0.67±0.02	13.2±0.2	0.22±0.02	1.92±0.03
RGO	0.74±0.02	13.0±0.1	0.39±0.01	3.71±0.05
Pt	0.76±0.01	12.5±0.2	0.74±0.01	7.00±0.04

45

device. To improve the performance of DSCs based on Fe_3O_4@RGO-NMCC CEs, TiO$_2$ photoanodes were optimized by TiCl$_4$ treatment. This optimization resulted in a PCE of 9.04%, nearly approaching 9.46% obtained from DSCs based on 50 pyrolytic Pt CEs (Figure 2b).

Cyclic voltammetry (CV) curve and Tafel polarization curve were obtained to study the catalytic performance and electron transfer in these CEs. Figure 2c shows the cyclic voltammograms of the I^-/I_3^- redox couple based on Fe_3O_4, RGO, Fe_3O_4@RGO-

NMCC, and Pt. The peak current of Fe_3O_4 CEs in CV was extremely small, indicating that massive interparticle boundaryadversely affected electron transport. This poor electron transport was bound to cause the absence of redox peaks for I^-/I_3^-
5 redox couple. This finding confirmed the results of our J–V curve analysis. Three curves based on RGO, Fe_3O_4@RGO-NMCC, and Pt CEs exhibited two pairs of redox peaks. The redox peak at low potential was attributed to the reaction: $I_3^- + 2e^- \leftrightarrow 3I^-$. The separation between the anodic and cathodic peaks (ΔE) was
10 inversely related to the rate of the above redox reaction and regeneration rate of I^-/I_3^- redox couple. The ΔE value for Fe_3O_4@RGO-NMCC CEs (104 mV) was significantly smaller than that for RGO (280 mV) and Pt (126 mV), implying notable catalytic behaviors for the reduction of I_3^- or I_2 into I^-. Although
15 Fe_3O_4@RGO CE had higher cathodic peak current density and smaller ΔE than those of Pt reference, its redox potential (E_R) (0.23V vs Ag/AgCl) is lower than that of Pt CE (0.29 V vs Ag/AgCl), which caused Fe_3O_4@RGO CE delivered a low PCE of 9.04% compared to that of Pt reference (9.46%) in Figure 2b.
20 The peak current of RGO in CV was relatively large, indicating that electron transfer readily occurred. However, the redox peak was not prominent, indicating few surface catalytic sites. Using symmetrical cells consisting of two identical CEs, Tafel polarization curves were measured as shown in the Figure 2d.
25 Among the four CEs, Fe_3O_4 CEs showed the least limited exchange current density, which again demonstrated that massive interparticle boundary detrimentally affected electron transfer. For Fe_3O_4@RGO-NMCC symmetrical cells, the charge transfer in Tafel zone was remarkably higher than that of Fe_3O_4 and RGO,
30 indicating superior catalytic activity. This finding was in good agreement with the CV measurements. Thus, the Fe_3O_4@RGO-NMCC not only increased the catalytic activity but also

accelerated electron transfer between the interfaces, which in turn increased the performance of the corresponding DSCs.
35 The development of flexible electrodes is the main research direction of current and future portable and curved electronic devices.[19-21] Flexible Fe_3O_4@RGO-NMCC CEs were prepared on polyethylene naphthalate/indium tin oxide plastic substrate, employing flexible Pt CEs (prepared by chemical reduction) as
40 reference. The J-V curves of DSCs based on flexible CEs are shown in Figure 3a. DSCs based on flexible Fe_3O_4@RGO-NMCC CEs gave PCEs of 8.0%, which was higher than that of DSCs based on flexible Pt (7.35%), which could be attributed to the higher photocurrent density of DSCs based on flexible
45 Fe_3O_4@RGO-NMCC CEs. Figure 3b shows the incident-photon-to-current conversion efficiency for DSCs based on flexible Fe_3O_4@RGO-NMCC and Pt CEs. The integrated currents for DSCs based on flexible Fe_3O_4@RGO-NMCC and Pt CEs were 15.30 and 11.76 mA cm^{-2}, respectively, agreeing with the J–V
50 results. As for rigid DSCs system, Fe_3O_4@RGO CE delivered a low PCE of 9.04% compared to that of Pt reference (9.46%) in Figure 2b, whereas the DSCs based on flexible Fe_3O_4@RGO CE gave a larger PCE than Pt. The reason for these results was attributed to the different preparing method of Pt on rigid
55 FTO/glass and flexible PEN/ITO substrate. The Pt on rigid FTO/glass was prepared by high-temperatures pyrolytic method, whereas Pt on flexible PEN/ITO substrate was prepared by chemical reduction method because of instability of the flexible plastic substrate at the high temperature (›150ºC). To confirm
60 superior performance of flexible Fe_3O_4@RGO CE to flexible Pt on PEN/ITO substrate, Tafel-polarization and CV and electrochemical impedance spectroscopy (EIS) were carried out to reveal catalytic activity and electron transport of flexible CEs.
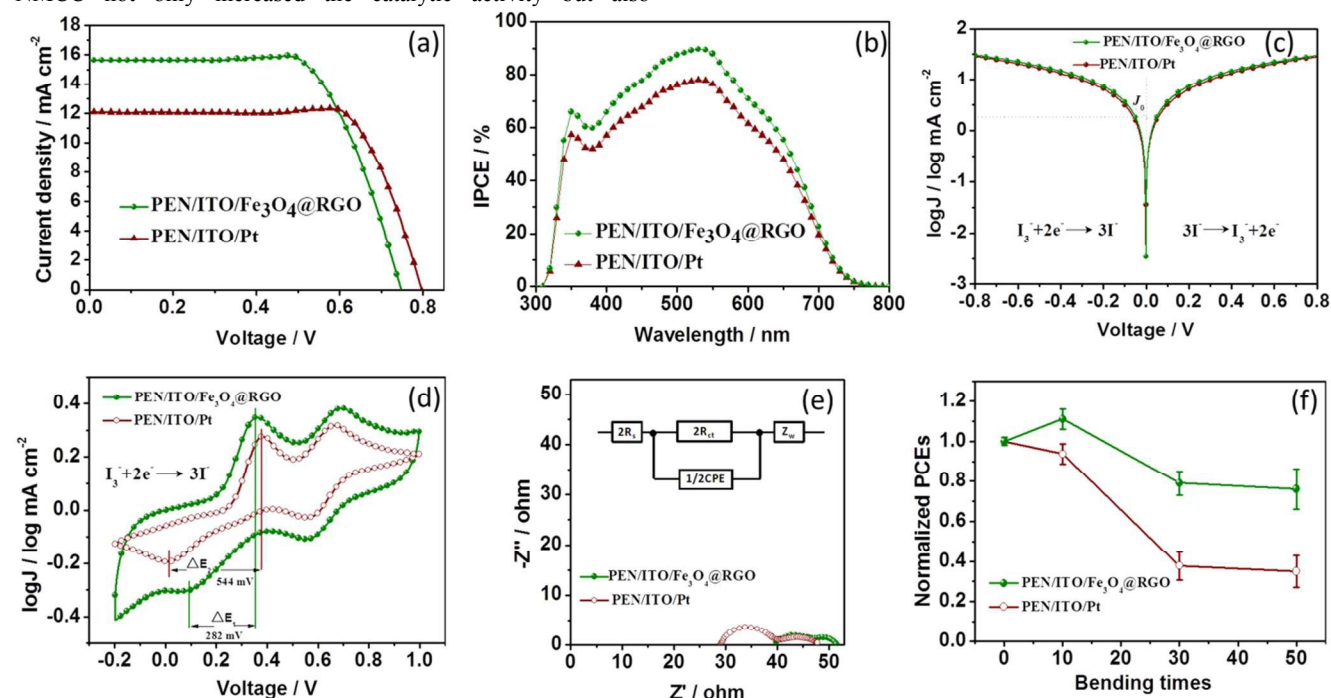
65 **Figure 3.** Photovoltaic and electrochemical properties characterization of CEs fabricated on flexible PEN/ITO substrate: (a) J-V curves of DSCs based on different flexible CEs; (b) IPCE of DSCs based on different flexible CEs; (c) Tafel polarization curves of the I_3^-/I^- symmetrical cells; (d) CV curves of various flexible CEs in I_3^-/I^- electrolyte; (e) electrochemical impedance spectroscopy of the I_3^-/I^- symmetrical cells; (f) PCE variations after 50 times bending randomly selected two flexible CEs around one pen with a diameter of 1cm.

Table 2. Photovoltaic parameters of the DSCs based on flexible CEs and EIS parameters of the symmetrical cells based on flexible CEs

Flexible CEs	V_{oc}(V)	J_{sc} (mA/cm^2)	J_{sc} (mA/cm^2) From IPCE	FF	PCE(%)	R_s (Ω)	R_{ct} (Ω)
PEN/ITO/Fe$_3$O$_4$@RGO	0.75±0.01	15.63±0.2	15.30±0.2	0.69±0.01	8.0±0.02	19.6±0.5	3.85±0.5
PEN/ITO/Pt	0.80±0.02	12.10±0.1	11.76±0.2	0.76±0.01	7.35±0.01	14.6±0.5	4.50±0.6

The exchange current density (J_0) (Figure 3c) for flexible Fe$_3$O$_4$@RGO-NMCC CEs (1.61 mA cm^{-2}) was significantly higher than that for Pt (1.36 mA cm^{-2}), implying its faster electron transfer than that of flexible Pt CEs. The ΔE value for flexible Fe$_3$O$_4$@RGO-NMCC (282 mV) CEs was significantly less than that for Pt (544 mV), implying its superior catalytic behavior to flexible Pt CEs. EIS was used to reveal the inherent interface resistance, with the results shown in Figure 3e. Meanwhile, an equivalent circuit diagram (Figure 3e, inset) is provided for fitting Nyquist plots with the Z-view software. Each plot comprised two irregular semicircles, with the first one originating from the charge transfer resistance (R_{ct}) at the CE/electrolyte interface. By contrast, the second semicircle arises from the Nernst diffusion impedance (Z_N) of I$_3^-$/I$^-$ within electrolyte. Usually, R_{ct} occurs in the high frequency region, whereas the Z_N appears in the low frequency region. In addition, the value intercepted on the real axis of Nyquist plot was attributed to the series resistance (R$_s$). Fitting results of Nyquist plots are listed in Table 2, which showed that R_{ct} of DSCs based on flexible Fe$_3$O$_4$@RGO-NMCC CEs (3.85 Ω) was smaller than

Figure 4. Stability of DSCs based on Fe$_3$O$_4$@RGO-NMCC CEs on FTO substrate. (25℃, 30% humidity, encapsulation, AM 1.5, 100 mW cm^{-2})

that of flexible Pt CE (4.50 Ω). Smaller charge transfer resistance based on flexible Fe$_3$O$_4$@RGO-NMCC CEs facilitated electron transfer. Suitable electron transfers are highly relevant to their structural advantages, e.g., electron hopping between Fe^{2+} and Fe^{3+}. Electrons were transported freely along a broad two-dimensional conductive surface based on RGO. Thus, superior catalytic activity and faster electron transport of flexible

Fe$_3$O$_4$@RGO CEs enhanced the photocurrent density of the corresponding DSCs. Bending tests (Figure 3f) indicated that the PCE of DSCs based on flexible Fe$_3$O$_4$@RGO-NMCC CEs could maintain 80% of their initial PCE after bending 50 times. However, the performance of DSCs based on flexible Pt CEs was notably decreased after bending 50 times. As we all known, two-dimensional material or its thin film has better mechanical flexibility than that of nanoparticles. We ascribed the deterioration in the performance of DSCs based on flexible Pt CE after bending to its mechanical brittleness (the crack defects on flexible Pt CE produced by repeated bending). Considering their photovoltaic and anti-bending performance, flexible Fe$_3$O$_4$@RGO-NMCC CEs are ideal. The stability test of DSCs based on Fe$_3$O$_4$@RGO-NMCC CEs was conducted as shown in Figure 4. After 2,000 h, DSCs based on Fe$_3$O$_4$@RGO-NMCC CEs maintained 60% of initial PCE.

Conclusions

In summary, we report the generation of nano-micro composite catalysts made of highly dispersed Fe$_3$O$_4$ nanoparticles fixed on RGO sheets as CE in DSCs using a simple one-pot solvothermal approach. Compared with pure Fe$_3$O$_4$ and RGO CEs, Fe$_3$O$_4$@RGO-NMCC CE exhibited superior electrocatalysis for the catalytic reduction of I$^-$/I$_3^-$ redox couple. Notably, DSCs using rigid and flexible Fe$_3$O$_4$@RGO-NMCC CEs achieved high PCEs reaching 9% and 8% on FTO/glass substrates and flexible polymer substrates, respectively. These values are the highest reported efficiencies for DSCs based on a flexible Pt-free CE. We ascribed the notable catalytic performance of Fe$_3$O$_4$@RGO-NMCC to faster electron hopping between Fe^{2+} and Fe^{3+} and free electron transport by broad electron transport-sheets of RGO. Finally, Fe$_3$O$_4$@RGO-NMCC exhibited good anti-bending and stability in practical application of DSCs.
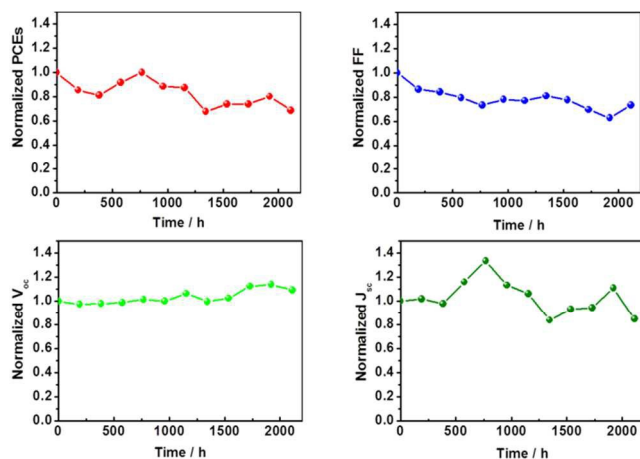
Acknowledgements

Notes and references

^{a} Shandong Provincial Key Laboratory of Chemical Energy Storage and

Novel Cell Technology, School of Chemistry and Chemical Engineering, Liaocheng University, Liaocheng 252059, China.
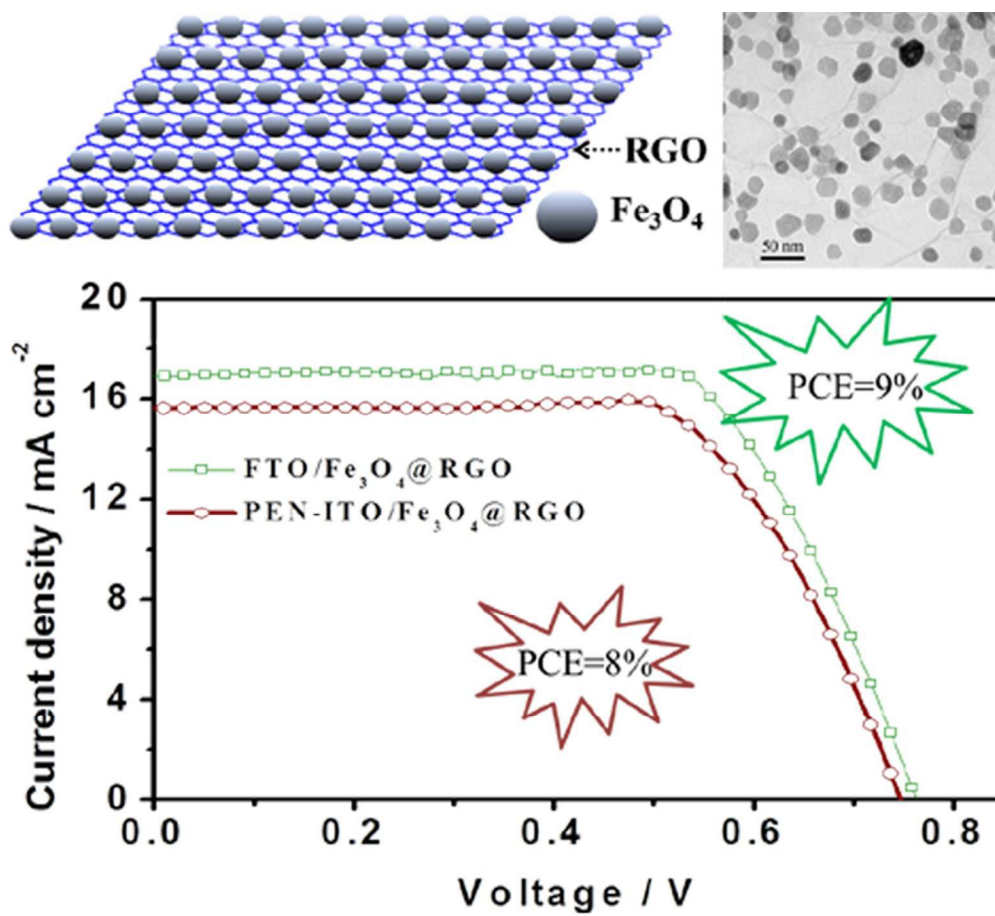*b College of Materials Science and Engineering, Liaocheng University, Liaocheng 252059, Shandong, China.*
5 *c Mössbauer Effect Data Center, Dalian Institute of Chemical Physics, Chinese Academy of Sciences, Dalian 116023, China.*
d Graduate School of Life Science and Systems Engineering, Kyushu Institute of Technology, 2-4 Hibikino, Wakamatsu, Kitakyushu, Fukuoka, 808-0196, Japan.
10 * Corresponding authors: yinjieily@163.com*

1.   B. Oregan and M. Gratzel, *Nature*, 1991, **353**, 737-740.
2.   S. Mathew, A. Yella, P. Gao, R. Humphry-Baker, B. F. E. Curchod, N. Ashari-Astani, I. Tavernelli, U. Rothlisberger, M.
15   K. Nazeeruddin and M. Graetzel, *Nat. Chem.*, 2014, **6**, 242-247.
3.   M. J. Ju, J. C. Kim, H. -J. Choi, I. T. Choi, S. G. Kim, K. Lim, J. Ko, J. -J. Lee, I. -Y. Jeon, J. -B. Baek, H. K. Kim, *ACS Nano*, 2013, 7, 5243–5250.
20 4.   M. J. Ju, I. -Y. Jeon, K. Lim, J. C. Kim, H. -J. Choi, I. T. Choi, Y. K. Eom, Y. J. Kwon, J. Ko, J. -J. Lee. Adv. Mater. 2014, 26, 3055-3062.
5.   M. K. Wang, A. M. Anghel, B. Marsan, N. L. C. Ha, N. Pootrakulchote, S. M. Zakeeruddin and M. Gratzel, *J. Am.
25   Chem. Soc.*, 2009, **131**, 15976-15977.
6.   M. Wu, X. Lin, Y. Wang, L. Wang, W. Guo, D. Qu, X. Peng, A. Hagfeldt, M. Graetzel and T. Ma, *J. Am. Chem. Soc.*, 2012, **134**, 3419-3428.
7.   A. Kay and M. Gratzel, *Sol. Energy Mater. Sol. C.*, 1996, **44**,
30   99-117.
8.   M. Wu, X. Lin, T. Wang, J. Qiu and T. Ma, *Energy Environ. Sci.*, 2011, **4**, 2308-2315.
9.   M. J. Ju, I. -Y. Jeon, K. Lim, J. C. Kim, H. -J. Choi, I. T. Choi, Y. K. Eom, Y. J. Kwon, J. Ko, J. -J. Lee, J. -B.
35   Baek, H. K. Kim, Energy Environ. Sci., 2014, 7, 1044-1052.
10.   X. Meng, C. Yu, X. Song, Y. Liu, S. Liang, Z. Liu, C. Hao J. Qiu, Adv. Energy Mater., 2015, 5, DOI: 10.1002/aenm.201500180.
11.   T. Yohannes and O. Inganas, *Sol. Energy Mater. Sol. C.*, 1998,
40   **51**, 193-202.
12.   Q. Li, J. Wu, Q. Tang, Z. Lan, P. Li, J. Lin and L. Fan, *Electrochem. Commun.*, 2008, **10**, 1299-1302.
13.   Y. Hou, D. Wang, X. H. Yang, W. Q. Fang, B. Zhang, H. F. Wang, G. Z. Lu, P. Hu, H. J. Zhao and H. G. Yang, *Nat.
45   Commun.*, 2013, **4**,1583.
14.   L. Wang, Y. Shi, H. Zhang, X. Bai, Y. Wang and T. Ma, *J. Mater. Chem. A*, 2014, **2**, 15279-15283.
15.   Qi. Yu, L. A. Jauregui, W. Wu, R. Colby, J. Tian, Z. Su, H. Cao, Z. Liu, D. Pandey, D. Wei, T. F. Chung, P.
50   Peng, N. P. Guisinger, E. A. Stach, J. Bao, S.-S. Pei, Y. P. Chen, *Nat. Mater.*, 2011, **10**, 443–449.
16.   D. Dimos, P. Chaudhari, J. Mannhart. *Phys. Rev. B*, 1990, **41**, 4038.
17.   L. Wang, Y. Shi, Y. Wang, H. Zhang, H. Zhou, Y. Wei, S.
55   Tao and T. Ma, *Chem. Commun.*, 2014, **50**, 1701-1703.
18.   S. W. Lee, S. J. Kim, I. B. Shim, S. Bae and C. S. Kim, *Ieee Transactions on Magnetics*, 2005, **41**, 4114-4116.
19.   H. Zhou, Y. Shi, D. Qin, J. An, L. Chu, C. Wang, Y. Wang, W. Guo, L. Wang and T. Ma, *J. Mate. Chem. A*, 2013, **1**,
60   3932-3937.
20.   H. Zhou, Y. Shi, K. Wang, Q. Dong, X. Bai, Y. Xing, Y. Du and T. Ma, *J. Phys. Chem. C*, 2015, **119**, 4600-4605.
21.   L. Li, Z. Wu, S. Yuan and X.-B. Zhang, *Energy Environ. Sci.*, 2014, **7**, 2101-2122.

71x64mm (300 x 300 DPI)